Published February 28, 2019

Original Research

Core Ideas

- Spontaneous imbibition was measured in rock fractures using neutron radiography.
- Early-time uptake of water displacing air showed a square root of time dependency.
- Fracture sorptivity was quantified from the slope of the early-time uptake data.
- Fracture sorptivity increased with increasing fracture aperture width.
- Fracture sorptivity decreased with increasing fracture surface roughness.

Rock Fracture Sorptivity as Related to Aperture Width and Surface Roughness

J.W. Brabazon, E. Perfect,* C.H. Gates, H.Z. Bilheux, J.S. Tyner, L.D. McKay, and B.B. Horodecky

Fractures in low-porosity rocks can provide conduits for fluid flow. Numerous researchers have investigated fluid flow through fractures under saturated conditions. However, relatively little information exists on spontaneous imbibition in fractures, whereby a wetting fluid displaces a non-wetting fluid by capillarity. We investigated spontaneous imbibition of water displacing air in a suite of fractured low-porosity sedimentary and igneous rock cores (5.08-cm length by 2.54-cm diameter). Mode I fractures were induced in the cores by compression between opposing parallel flat plates. The following physical properties were measured: bulk density, ρ_b; solid-phase density, ρ_s; porosity, ϕ; contact angle, θ_e; fracture aperture width, $x_{geo;}$ and fracture surface roughness, W_r. The wetting front in each fracture was imaged using dynamic neutron radiography. Early-time uptake exhibited a square root of time dependency, and was quantified by linear regression, with the slope equal to the fracture sorptivity, S_f. Estimates of S_f ranged from 10.1 to 40.5 mm $s^{-0.5}$, with a median value of 25.0 mm $s^{-0.5}$. There was a statistically significant effect of rock type on S_f, with igneous rocks generally having lower mean values than sedimentary rocks. Differences in ρ_b, ρ_s, ϕ, and θ_e between the rock types did not contribute significantly to the variation in S_f. However, x_{geo} and W_r were significantly correlated with S_f. These correlations indicated that S_f increases with increasing x_{geo}, as predicted by early-time capillary theory, and decreases with increasing W_r, analogous to the decrease in fracture permeability with increasing surface roughness observed under saturated flow conditions.

Abbreviations: ANOVA, analysis of variance; BL, Burlington Limestone; CS, Crossville Sandstone; FOV, field of view; HSD, honestly significant difference; MS-par, Mancos Shale cored parallel to bedding; MS-per, Mancos Shale cored perpendicular to bedding; SW, Sierra White Granite; VBA, Vermilion Bay Granite A; VBB, Vermilion Bay Granite B; WG, Westerly Granite.

J.W. Brabazon, E. Perfect, C.H. Gates, L.D. McKay, and B.B. Horodecky, Dep. of Earth and Planetary Sciences, Univ. of Tennessee, Knoxville, TN 37996; H.Z. Bilheux, Instrument and Source Division, Oak Ridge National Lab., Oak Ridge, TN 37831; J.S. Tyner, Dep. of Biosystems Engineering and Soil Science, Univ. of Tennessee, Knoxville, TN 37996. *Corresponding author (eperfect@utk.edu).

Received 19 Aug. 2018.
Accepted 7 Dec. 2018.

Citation: Brabazon, J.W., E. Perfect, C.H. Gates, H.Z. Bilheux, J.S. Tyner, L.D. McKay, and B.B. Horodecky. 2019. Rock fracture sorptivity as related to aperture width and surface roughness. Vadose Zone J. 18:180156. doi:10.2136/vzj2018.08.0156

Low-porosity rocks, such as granites, marbles, and shales, tend to inhibit the flow of fluids in the subsurface. However, fractures in these rocks can provide passageways for flow and transport. Numerous researchers have studied the movement of fluids through fractures under saturated conditions (e.g., Kanematsu et al., 2009; Karpyn et al., 2009; Rangel-German and Kovscek, 2002). However, relatively little research has been done on the hydraulic properties of fractured low-porosity rocks under partially saturated conditions.

In multiphase porous media, a physicochemical phenomenon known as spontaneous imbibition has the potential to drive fluid flow. Spontaneous imbibition occurs when a wetting phase fluid (e.g., water or brine) moves into a porous medium, displacing a pre-existing non-wetting fluid (e.g., air, natural gas, or oil). This process is attributable to capillary action within the voids (Morrow and Mason, 2001; Schmid and Geiger, 2012). In low-porosity rocks, the wetting fluid invades individual fractures much faster at early times than pores in the surrounding matrix (Cheng et al., 2015).

This phenomenon has a number of important practical implications. In the vadose zone, it contributes to water fluxes and increases the dispersion of solutes (Schmid et al., 2011). Geochemical weathering of granitic rocks has been shown to occur more readily when water is able to permeate the matrix through interconnected fracture networks (Rossi and Graham, 2010; Navarre-Sitchler et al., 2015). Similarly, spontaneous imbibition can

damage building foundations and other engineered structures by facilitating repeated wetting within micro-cracks (Şahmaran and Li, 2009). In fact, the rate of water uptake by spontaneous imbibition has been proposed as a measure of construction material durability (Lockington et al., 2002).

Geological repositories are increasingly being used to contain harmful or unwanted substances such as CO_2 and radioactive waste. Repositories generally consist of natural geologic barriers bounding a porous storage formation (Suzuki et al., 2018; Gaurina-Međimurec and Mavar, 2017). Often, an overlying low-porosity, low-permeability layer, referred to as *caprock*, is crucial to the containment of the waste. A fractured caprock could allow sequestered waste to escape by spontaneous imbibition. In geologic carbon sequestration, a detailed risk assessment is performed to determine caprock integrity (IPCC, 2005).

For nuclear wastes, a combination of low-porosity rocks and engineered materials are used for deep storage (Suzuki et al., 2018). Radioactive materials are encapsulated in an engineered canister and emplaced in a shaft within a low-porosity host rock, typically a granite. A bentonite clay buffer is placed around the canister. The shaft is then backfilled with clay and host rock material. Lastly, a concrete plug is used to seal the entire storage location (Suzuki et al., 2018; Kim et al., 2011).

Fractures created during excavation, as well as the presence of preexisting natural fractures, can provide potential migration pathways. In the advent of leakage, such pathways could permit fluid flow by spontaneous imbibition, resulting in the transport of contaminated material (Gaurina-Međimurec and Mavar, 2017; Kim et al., 2011). Thus, a better understanding of spontaneous imbibition in fractured low-porosity rocks could help mitigate potential contamination and aid in the determination of suitable rock formations for deep waste repositories.

Spontaneous imbibition has long been used as a method for enhancing oil recovery in fractured conventional oil and gas reservoirs (Morrow and Mason, 2001; Rangel-German and Kovscek, 2002; Dehghanpour et al., 2013). Water is typically injected into a fractured reservoir with the intent of allowing spontaneous imbibition to displace the non-wetting phase (i.e., oil and gas) from the matrix. The displaced oil and gas can then enter fractures where these fluids are able to move much more easily (Rangel-German and Kovscek, 2002).

Spontaneous imbibition is also relevant to unconventional reservoirs such as tight gas shales and sandstones (Cui et al., 2014; Alfarge et al., 2017). The main method used in exploiting these reservoirs is hydraulic fracturing, also known as *fracking*. This method is based on horizontal drilling, and involves the injection of large volumes of water, chemical additives, and suspended solids (*proppants*) into the subsurface under high pressures (Osiptsov, 2017). As a result, fractures are induced within the source rocks, increasing their overall permeability (Li et al., 2015). Often, only a small fraction of the injected fracturing fluid is recovered (Ghanbari and Dehghanpour, 2016). The lost fluid, known as *leak-off*, contributes to the overuse of water resources (Vengosh et al., 2014). Leakoff is greatly increased for wells with an extended shut-in time, and this has been attributed to spontaneous imbibition of the fracturing fluid into the matrix (Ghanbari and Dehghanpour, 2016; Dehghanpour et al., 2013).

Only a few researchers have previously experimentally investigated spontaneous imbibition within fractured porous media. These studies used either the traditional gravimetric method or neutron imaging to measure water uptake within discrete fractures. Şahmaran and Li (2009) measured spontaneous imbibition in engineered cementitious composites. Rates of uptake increased dramatically as the number of micro-cracks induced by mechanical loading increased. Hall (2013) studied spontaneous imbibition of water within a fractured sandstone, comparing uptake in the fractures themselves with that in the surrounding matrix. Cheng et al. (2015) quantified water uptake within individual fractures in mechanically fractured sandstone cores. Recently, Bao and Wang (2017) and DiStefano et al. (2017) have reported measurements of capillary flow within artificial cracks created in granite and shale samples, respectively.

Early-time capillary theory predicts higher rates of water uptake with increasing fracture aperture width (Cheng et al., 2015; Shi et al., 2018). While some of the experimental studies discussed above also measured aperture width, a definitive validation of this theoretical relationship is still lacking. Moreover, none of them looked at the effect of fracture surface roughness on spontaneous imbibition.

We were unable to locate any previous research on the influence of fracture surface roughness on capillary uptake. However, many studies have focused on the influence of fracture surface roughness on steady-state fluid flow under saturated conditions (e.g., Koyama et al., 2008; Huang et al., 2017). Huang et al. (2018) noticed that the tortuous flow path inside rough fracture shear bands greatly reduces permeability. Similarly, Brown (1987) reported that flow through fractures with rough surfaces yielded flow rates of between 70 and 90% of those estimated from models based on smooth parallel plate geometry. We anticipate that these trends will also apply to spontaneous imbibition in fractures.

In this study, we sought to extend previous research by measuring spontaneous imbibition on a suite of fractured low-porosity sedimentary and igneous rocks. The main goal was to image water displacing air within individual fractures and to relate any observed differences between rock types to their physical properties. The specific objectives were to: (i) characterize physical properties of the matrix and Mode I fractures induced by compression between opposing parallel flat plates; (ii) visualize spontaneous imbibition of water within the induced fractures; and (iii) quantify and relate rates of water uptake to physical properties.

The specific hypotheses to be tested included: (i) mean values of the various physical properties measured differ between rock types; (ii) the wetting front in the fracture advances with the square-root of time; (iii) rates of water uptake differ between rock types; and (iv) differences in rates of water uptake can be related to differences in matrix and fracture physical properties.

Materials and Methods

Rock Types and Core Preparation

A suite of low-porosity rock cores were acquired from a commercial vendor, Kocurek Industries (Caldwell, TX). The cylindrical cores came from surface outcrops with unknown locations. Their dimensions were 5.08 cm long by 2.54 cm in diameter. Bulk density, ρ_b, solid-phase density, ρ_s, and He gas porosity, ϕ, of selected oven-dried cores were measured using the methods of Donnelly et al. (2016), with core volume calculated from core length and diameter.

The cores consisted of both sedimentary and igneous rock types. The sedimentary rock types were Burlington Limestone, Crossville Sandstone, and Mancos Shale. The igneous rock types were Sierra White Granite, Vermilion Bay Granite, and Westerly Granite. Several cores of each rock type were obtained, allowing subsequent statistical analysis.

Burlington Limestone (known commercially as Carthage Marble) is a medium-grained, gray to brown, marine limestone that was laid down in the Mississippian period. It is present in Illinois, Iowa, and Missouri. According to Kocurek Industries, the permeability of Burlington Limestone varies between 4×10^{-18} and 7×10^{-18} m^2. Crossville Sandstone (known commercially as Crab Orchard Sandstone) was deposited during the Pennsylvanian period and is located in Kentucky and Tennessee. It is a light-gray, fine- to medium-grained sandstone with bands of yellow, brown, and red due to iron staining (Wanless, 1946). Gehne and Benson (2017) measured the permeability of Crossville Sandstone with values ranging between 3×10^{-18} and 3×10^{-17} m^2. Mancos Shale is an interbedded siltstone and shale located in New Mexico, Wyoming, and Utah that was deposited in the Late Cretaceous. According to Mokhtari and Tutuncu (2015), its permeability can vary between 9×10^{-19} and 3×10^{-17} m^2. The Mancos Shale was cored both parallel and perpendicular to the bedding. The cores were gray in color with light gray interbedding.

Sierra White Granite was emplaced in the Sierra Nevada in California between the Permian and Tertiary periods. The permeability of this granite has been reported to range from 5×10^{-19} to 1×10^{-18} m^2 (Ye and Ghassemi, 2018). Vermilion Bay Granite is a fine- to medium-grained, deep pink to light red, alkali granite from northwestern Ontario, Canada. It dates from the Grenville orogeny. No published information could be found on the permeability of this granite. Two commercial variants were investigated: Morning Rose and North American Pink, designated as Vermilion Bay Granite A and B, respectively. Westerly Granite is a fine-grained, gray to light gray granite from Rhode Island. It was probably emplaced in the Pennsylvanian period. Brace et al. (1968) report a permeability of 6×10^{-20} m^2 for Westerly Granite.

The following abbreviations are used to identify the different rock types: Burlington Limestone (BL), Crossville Sandstone (CS), Mancos Shale (MS) cored parallel (MS-par) and perpendicular (MS-per) to bedding (MS-per), Sierra White Granite (SW), Vermilion Bay Granite A (VBA), Vermilion Bay Granite B (VBB), and Westerly Granite (WG).

The sides of selected rock cores were wrapped with Kapton tape to keep them intact during fracturing and provide no-flow boundaries during the spontaneous imbibition experiments. The wrapped cores were fractured following the Brazilian method (Li and Wong, 2013, Cheng et al., 2015) using a Carver laboratory press (Model M) with a 25-ton hydraulic unit (Model no. 3925). Other than being wrapped in Kapton tape, the rock cores were not subjected to any confining pressure. Each core was placed longitudinally between opposing flat parallel loading plates, and a Mode I fracture was induced by applying stress until failure; a typical example is shown in Fig. 1. Between four and nine (median eight) replicate fractured cores were prepared per rock type.

Dynamic Neutron Radiography

Prior to neutron imaging, the wrapped, fractured cores were oven dried at 105°C for a period of 24 h to bring each sample to zero initial moisture content. They were then placed in sealed containers to minimize changes in their moisture content with time until immediately before the spontaneous imbibition measurements.

Two-dimensional spontaneous imbibition data were obtained for each core in the form of the height of wetting within the fracture zone vs. elapsed time. Neutron imaging is a novel way to obtain these data due to its ability to visualize and quantify the uptake of water within an individual fracture at reasonable frame rates (Perfect et al., 2014; Cheng et al., 2015). Dynamic neutron radiography was performed at the Neutron Imaging Facility (beamline CG-1D, High-Flux Isotope Reactor) of Oak Ridge National Laboratory. Data were collected in May 2017 utilizing the microchannel plate detector. This detector has a pixel size of 55 by 55 μm^2 and a field of view (FOV) of 28 by 28 mm^2. The detector yielded a relatively consistent frame rate of about six frames per second.

The oven-dried cores were individually placed in front of the microchannel plate detector with their fracture planes oriented parallel to the neutron beam. Each core was imaged as its base

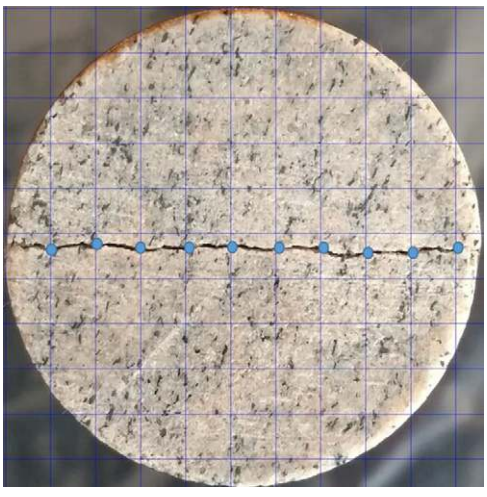

Fig. 1. Top view of a Westerly Granite core showing the Mode I fracture and a superimposed grid. Aperture width measurements were made at the intersections of the grid with the fracture, as indicated by the solid blue circles.

was brought into contact with a deionized-water reservoir (Fig. 2a). The resulting imbibition within the fracture zone was visualized as a series of time-stamped radiographs.

Image stacks from each core were analyzed in ImageJ (Schneider et al., 2012). The images were first normalized by dividing each image in the time sequence by the initial image before water contacted the base of the core. The normalized images allow visible delineation of the wetting front within the fracture zone at any given time (see Fig. 2b). For each image in the normalized sequence, fracture water uptake was measured, yielding the height of wetting. In this way, between 3 and 11 (median = 6) pairs of wetting height vs. time values were obtained for each core. For the low-porosity rock types investigated here, water movement into the matrix was negligible during the 1- to 2- s time frame needed to capture the dynamics of spontaneous imbibition within the fracture zone.

Fracture Sorptivity Estimation

Sorptivity has been shown to be a useful parameter for quantifying rates of water uptake at both the small, individual-pore, scale and at larger Darcian, multiple-pore, scales (Hall, 1989; Taha et al., 2001; Lockington et al., 2002; Cheng et al., 2015). We estimated the fracture sorptivity, S_f, from the dynamic neutron radiography data using Philip's equation (Philip, 1957; Cheng et al., 2015):

$$h = S_f \sqrt{t} \quad [1]$$

where h is the height of wetting and t is time. Equation [1] ignores the influence of gravity and thus is only applicable to early-time data, such as those collected in the present study.

For each core, the height of wetting data were linearly regressed against the square root of time, with the regression model forced through the origin (R Core Team, 2016). The S_f was then obtained from the slope of the best-fit regression line (Culligan et al., 2005; Taha et al., 2001). We used the coefficient of determination, R^2, to evaluate the strength of the linear relationship between h and $\sqrt{t}$. If the R^2 was <0.9, then the resulting S_f estimate was excluded from further analyses.

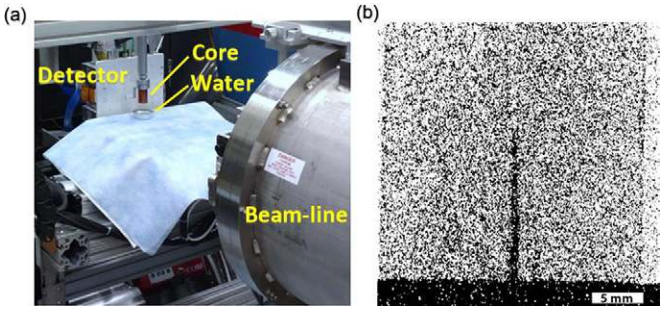

Fig. 2. (a) Neutron imaging setup, in which a water reservoir (aluminum container) is brought into contact with the base of a rock core (brown) in the neutron beam line while the micro-channel plate detector images neutrons attenuated by the water; and (b) normalized neutron radiograph of a Crossville Sandstone core showing water (black) entering the fracture from the reservoir.

Fracture Aperture Width Measurements

Fracture apertures, acting somewhat like capillary tubes, probably influenced the rates of water imbibition into the cores. As seen in porous media, faster early-time imbibition of the wetting phase is seen in larger capillaries, while slower imbibition is seen in smaller capillaries (Shi et al., 2018). Thus, the aperture widths of all of the fractured cores were measured to account for this potential influence.

Digital images of both the top and bottom of each replicate fractured core were taken with a high-resolution camera. The aperture width of the visible fracture, x, was then measured at 10 locations on a randomly positioned superimposed square grid in ImageJ (Schneider et al., 2012) (see Fig. 1). The measurement resolution was 12 μm. A second randomly positioned grid was then superimposed on the image and the measurement process was repeated. Both the top and bottom images of each core were analyzed in this way, resulting in 40 measurements of x per core. It was assumed that the aperture distributions for the exposed ends of the cores represent those in the interior.

The frequency distributions of x were right skewed for all eight rock types (data not shown). Logarithmic transformation of these distributions indicated that the individual x values were lognormally distributed (Fig. 3). This finding is consistent with previous research on the variation in aperture widths along individual fractures (Keller, 1998; Konzuk and Kueper, 2004). Therefore, geometric mean aperture widths, x_{geo}, were computed for each core and used to characterize fracture size in the statistical analyses.

Fracture Surface Roughness Measurements

Increasing surface roughness has been shown to reduce fracture flow under saturated conditions (e.g., Brown, 1987). We hypothesized that it would also impact the rates of uptake due to spontaneous imbibition. Thus, surface roughness was measured on subsamples of the fracture faces to account for this possibility.

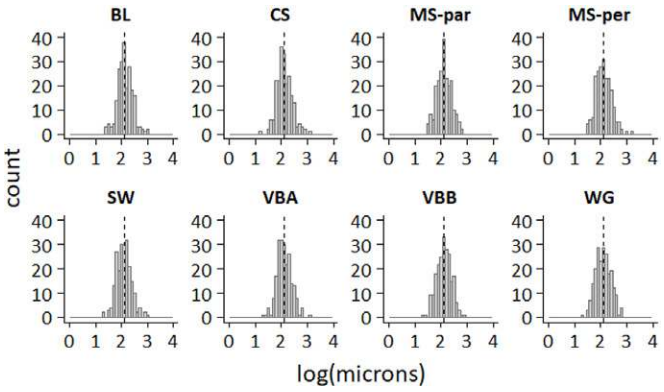

Fig. 3. Log-transformed frequency distributions for the individual measurements of the aperture width of the visible fracture, x, pooled for each rock type: Burlington Limestone (BL), Crossville Sandstone (CS), Mancos Shale, cored both parallel (MS-par) and perpendicular (MS-per) to bedding, Sierra White Granite (SW), Vermilion Bay Granite A (VBA), Vermilion Bay Granite B (VBB), and Westerly Granite (WG).

Replicate cores of each rock type were fractured using the Brazilian method (Li and Wong, 2013), as described above. The fractured cores were then unwrapped and separated into two halves, each with an exposed fracture face. Fragment subsamples of the rock fracture faces were created by compressive loading of the half cores. Each half core was positioned horizontally between opposing flat parallel loading plates, with the exposed fracture surface perpendicular to the plates. A Carver laboratory press (Model M) and 25-ton hydraulic unit (Model no. 3925) was then used to apply stress. As the load progressively increased, fragments of the exposed fracture surface flaked off and were collected. The average fragment size was 0.11 cm^3; a typical example is shown in Fig. 4a. Two half cores of each rock type were loaded, and three fragments were harvested from each fracture surface, yielding six fragments per rock type. It proved impossible to sample the MS-per half cores using this method, so only fragments from the MS-par half cores were collected and analyzed.

The fragments were cleaned with compressed air to remove any fault gouge and analyzed for surface roughness using a Phenom Pro X scanning electron microscope (Phenom-World BV). This instrument is capable of measuring surface heights with a vertical resolution of <10 nm. The fracture surface of each rock fragment was analyzed using three different FOVs: 200 by 200, 400 by 400, and 600 by 600 μm^2. The height maps for each FOV were exported as individual matrices of 512 by 512 pixels. An example height map is shown in Fig. 4b.

The height maps were analyzed for surface area using a MATLAB script by Richard Brown (MATLAB Answers). The script uses clockwise triangular meshing, which treats each set of four adjacent points as an independent quadrilateral cut into two triangles. Using the known spacing between points and corresponding height values, the area of each triangle is computed. The projected surface area of each height map was obtained by summing the areas of all the triangles. Fracture surface roughness was then quantified with the Wenzel roughness factor, W_r, as defined by (Wenzel, 1936)

$$W_r = \frac{A_R}{A_S} \quad [2]$$

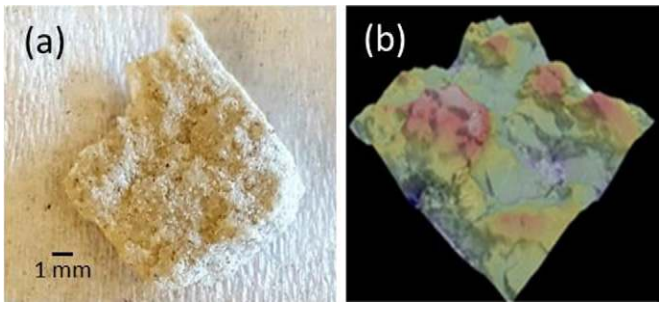

Fig. 4. (a) A typical fragment from an exposed fracture surface, and (b) height map for a 400- by 400-μm^2 field of view in which warm colors represent microtopographic highs and cooler colors represent elevational lows. Both examples are for Crossville Sandstone.

where A_R is the projected area of the rough surface relative to the corresponding area of the smooth flat surface, A_S, equivalent to the FOV. This factor has successfully been used to characterize surface roughness in several recent studies (e.g., Ramón-Torregrosa et al., 2008; Bizjak, 2010; Ai et al., 2017). Analysis of variance (ANOVA) performed on the calculated W_r values indicated no significant effect due to the different FOVs. Therefore, the W_r value for each fragment subsample was computed by averaging across all three FOVs.

Contact Angle Measurements

Unfractured replicate cores of the different rock types were cut into 1.27-cm long by 2.54-cm diameter disks. The cut surfaces of the disks were sequentially polished using successively finer grits, with 0.05-μm γ-alumina powder used to give a final mirror finish. Following oven drying, apparent equilibrium contact angles, θ_e, were measured for deionized water in the presence of air on the polished flat surfaces using a transient sessile drop method. A detailed description of this method was given in Gates et al. (2018). For Mancos Shale, the surfaces of the MS-par disks were too heterogeneous for contact angle measurements, so only the MS-per disks were analyzed.

Based on the mean W_r and θ_e values for each rock type, apparent equilibrium contact angles for the rough fracture surfaces, θ_r, were computed using the Wenzel (1936) model:

$$\cos\theta_r = W_r \times \cos\theta_e \quad [3]$$

In cases where the right-hand side of Eq. [3] was above unity when evaluated, a value of 0° was assigned following Onda et al. (1996).

Statistical Analyses

All statistical analyses were performed using either R (R Core Team, 2016) or the Analysis ToolPak in Microsoft Excel. Each measured variable was subjected to an ANOVA. The x_{geo} data were logarithmically transformed to satisfy ANOVA assumptions. Tukey's honestly significant difference (HSD) tests were used to compare the equivalency of mean values between pairs of rock types. Relationships between S_f and the independent variables x_{geo}, W_r, ρ_b, ρ_s, ϕ, θ_e, and θ_r were quantified using correlation or regression analyses. Those analyses were performed on individual core data for S_f vs. x_{geo} and on mean values for the different rock types for S_f vs. the other variables.

Results and Discussion

Measurements of the height of the wetting fluid within the fracture, acquired from the neutron radiographs, consistently portrayed a square-root-of-time behavior. A linear model, with a zero intercept, fitted these data very well (Fig. 5). Altogether, 36 data sets were fitted, of which seven were excluded from further analysis because their R^2 values were <0.90. The R^2 values for the remaining 29 data sets ranged from 0.904 to >0.999, with a median value of 0.982.

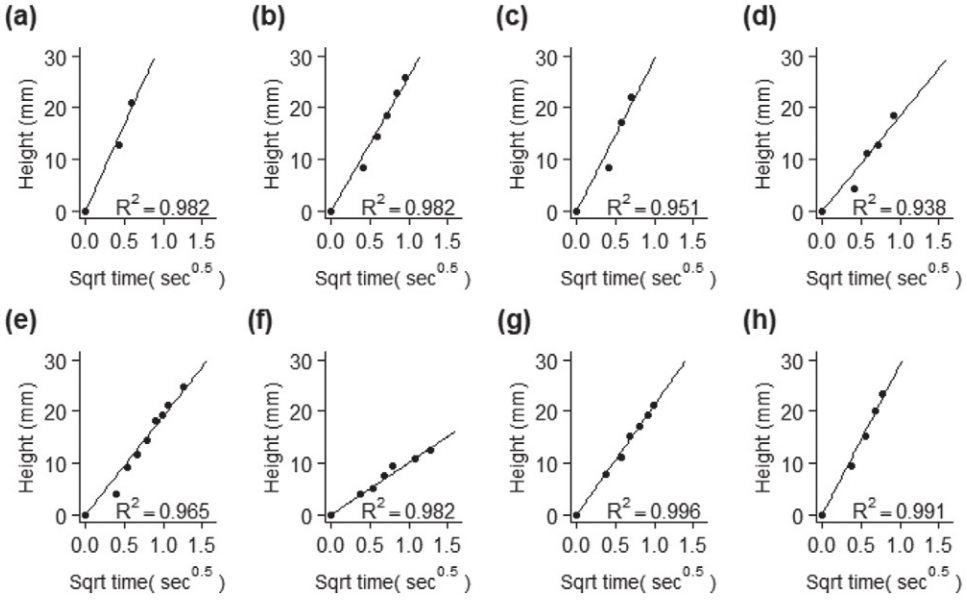

Fig. 5. Typical examples of a linear regression model fitted to wetting front height vs. the square root (Sqrt) of time for each rock type: (a) Burlington Limestone, (b) Crossville Sandstone, (c) Mancos Shale cored parallel to bedding, (d) Mancos Shale cored perpendicular to bedding, (e) Sierra White Granite, (f) Vermilion Bay Granite A, (g) Vermilion Bay Granite B, and (h) Westerly Granite.

Fracture sorptivity values were estimated from the slopes of the 29 regression models fitted to the wetting front height vs. square root of time data. The estimates ranged from 10.1 to 40.5 mm $s^{-0.5}$, with a median value of 25.0 mm $s^{-0.5}$. The S_f values were averaged across several replicate cores per rock type (Fig. 6). The ANOVAs indicated significant differences in mean fracture sorptivity values between rock types (at $p < 0.05$). Based on a Tukey HSD test, four groupings with statistically similar mean S_f values could be distinguished. In general, the igneous rocks (SW, VBA, and VBB) had lower mean S_f values than the sedimentary rocks (BL, CS, and MS). The sole exception was WG, which had a much higher mean fracture sorptivity than the other granites (Fig. 6).

Ignoring gravity, the theoretical sorptivity of a wetting fluid moving into the gap formed between two perfectly smooth, impermeable parallel plates, S_p, is given by (Schwiebert and Leong, 1996)

$$S_p = \frac{\xi \gamma \cos\theta_s}{3\mu} \quad [4]$$

where ξ is the separation distance between the two plates, γ is the surface tension of the liquid–vapor interface, θ_s is the equilibrium contact angle for an ideal flat surface, and μ is the absolute viscosity. Based on Eq. [4], S_p values were calculated for the different rock types; textbook values for μ and γ were input, while ξ and θ_s were equated with the mean values of x_{geo} and θ_e, respectively, in Table 1. The resulting S_p predictions ranged from 33.9 to 66.2 mm $s^{-0.5}$, with a median value of 41.3 mm $s^{-0.5}$. While these values are of the same order of magnitude as the experimentally determined S_f values, there was no significant correlation (at $p < 0.05$) between S_f and S_p, indicating that differences in fracture geometry and other physicochemical properties not accounted for in Eq. [4] play a key role in controlling water uptake.

Mean values of the various physical properties measured are given in Table 1. The ANOVAs indicated significant differences in mean values between rock types for all of the physical properties except θ_r. This property could not be analyzed by ANOVA because it was calculated using mean values of θ_e and W_r for each rock type in Eq. [3], hence there was no replication. For each physical property, Tukey HSD groupings are indicated by the letters following the mean values in Table 1.

The mean ρ_b values for the different rock types ranged from 2.50 g cm^{-3} for MS to 2.66 g cm^{-3} for BL. The BL also had the highest mean solid-phase density, 2.70 g cm^{-3}, with VBA having the lowest mean ρ_s value, 2.63 g cm^{-3}. The sedimentary rock types had the highest mean porosities (ranging from 1.77% for BL to 5.85% to CS), while the igneous rocks had the lowest mean values (ranging from 0.69% for VBA to 1.49% for SW). Three of the four granites studied had mean ϕ values <1%. There were no significant correlations between the rock density or porosity measurements and fracture sorptivity.

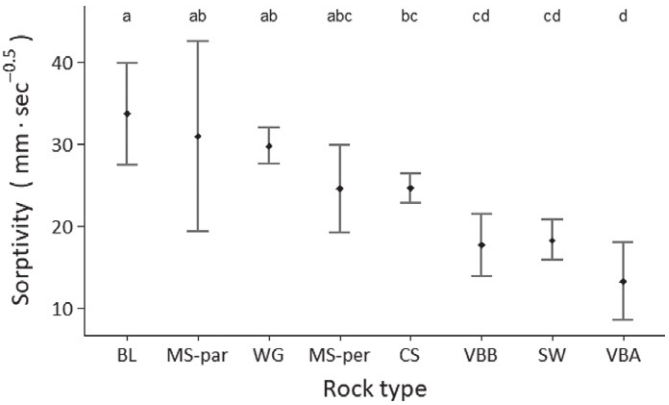

Fig. 6. Mean fracture sorptivity (black diamonds) with 95% confidence intervals for each rock type: Burlington Limestone (BL), Crossville Sandstone (CS), Mancos Shale, cored both parallel (MS-par) and perpendicular (MS-per) to bedding, Sierra White Granite (SW), Vermilion Bay Granite A (VBA), Vermilion Bay Granite B (VBB), and Westerly Granite (WG). Mean values for rock types with the same letter are not significantly different at $p < 0.05$ according to Tukey's honestly significant difference (HSD) test.

Table 1. Mean values of various physical properties measured on the suite of rock types investigated.

Rock type†	ρ_b	ρ_s	ϕ	x_{geo}	W_r	θ_e	θ_r
	g cm^{-3}		%	mm	m^2 m^{-2}	°	
BL	2.66A‡	2.70A	1.77B	191A,B	1.63A	75.6A	66.1
CS	2.50D	2.66B,C	5.85A	89D	1.62A	41.3C,D	0.0
MS	2.50D	2.64D	5.59A	85D§	1.76A,B¶	37.2D#	0.0
SW	2.63B	2.67B	1.49B	176A,B	1.84A,B	45.8C	0.0
VBA	2.61C	2.63E	0.69C	166A	1.88B	58.6B	11.6
VBB	2.62B,C	2.70D	0.81C	125C	1.82A,B	55.7B	0.0
WG	2.63B	2.65C,D	0.89C	205A	1.70A,B	52.2B	0.0

† BL, Burlington Limestone; CS, Crossville Sandstone; MS, Mancos Shale; SW, Sierra White Granite; VBA, Vermilion Bay Granite A; VBB, Vermilion Bay Granite B; WG, Westerly Granite.
‡ Mean values in same column followed by the same letter not significantly different according to Tukey's honestly significant difference (HSD) test.
§ Pooled geometric mean for MS cored both parallel (MS-par) and perpendicular (MS-per) to bedding; no significant difference between these core types.
¶ Mean is for MS-par only; this property was not measurable on MS-per.
# Mean is for MS-per only; this property was not measurable on MS-par.

The apparent equilibrium contact angles for the flat polished surfaces were averaged for each rock type studied. An ANOVA combined with a Tukey's HSD test indicated significant differences among the rock types (Table 1). Burlington Limestone had the highest mean θ_e value and was significantly less hydrophilic than the other rock types. Mancos Shale had the lowest θ_e value and was significantly more hydrophilic than the other rock types except for CS. The mean values of θ_e for the granites ranged from 45.8 to 58.6°, with the mean value for SW significantly lower than the mean values for the three alkaline granites, which were not significantly different from each other. Despite significant differences among the rock types, no significant relationship was found between θ_e and fracture sorptivity.

Inserting mean values for θ_e and W_r from Table 1 into Eq. [3], the apparent rough contact angle was calculated for each rock type. The results are shown in Table 1. It can be seen that most of the θ_r values were zero. A rough contact angle of 0° indicates complete wetting. Non-zero numbers for θ_r were obtained only for BL and VBA, indicating that their fracture surfaces were not completely wetting. These two rock types also had the highest θ_e values for the polished flat surfaces. The preponderance of zero values for θ_r in Table 1 suggests that this property was not particularly influential in determining the observed differences in fracture sorptivity.

Geometric mean fracture aperture widths for the individual cores ranged from 38 to 259 μm, with a median x_{geo} value of 127 μm. An ANOVA performed on the logarithmically transformed x_{geo} values indicated significant differences (at $p < 0.05$) among the rock types. Post hoc comparisons using the Tukey HSD test revealed four statistically similar groupings. The data were then back-transformed to give the results presented in Table 1.

The sedimentary rocks generally had narrower fracture aperture widths than the igneous rocks (Table 1). The sole exception was BL, which had wider fractures than the other sedimentary rocks and even the majority of the igneous rocks. There was no statistical difference between the x_{geo} values for the sandstone and shale cores. Among the igneous rocks, the x_{geo} value for WG was significantly larger than the values for the other granites. The differences in x_{geo} observed among the rock types may be related to their different porosities. There was a highly significant negative correlation between x_{geo} and ϕ ($r = -0.85$, $p < 0.01$), indicating that wider fractures were generally produced in lower porosity rocks. Porosity probably influences the rock mechanical properties that determine the width of an induced fracture during compressive loading.

When analyzed across all rock cores, there was no statistically significant relationship between x_{geo} and S_f. However, when separated into igneous and sedimentary groups, two positive relationships were revealed, with the regression model for the sedimentary rocks being statistically significant (Fig. 7). This resulted from the S_f values for the sedimentary rocks being larger than those for the igneous rocks, while this trend was reversed for the x_{geo} values. The existence of a positive relationship between S_f and

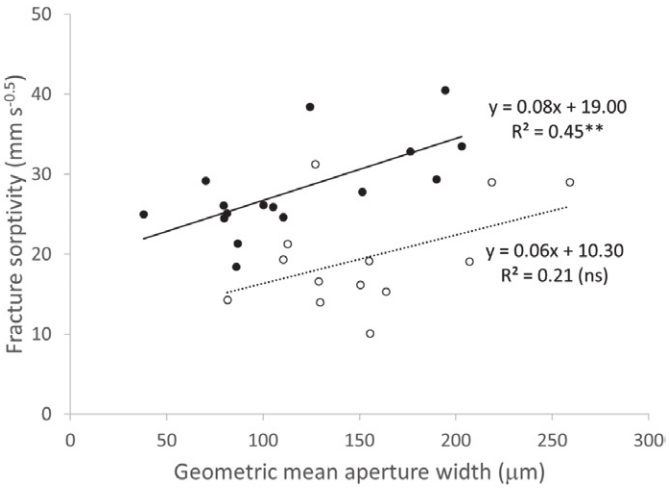

Fig. 7. Linear regression relationships between fracture sorptivity and geometric aperture width for the sedimentary (black circles with a solid line) and igneous (open circles with a dashed line) rock types.

x_{geo} is consistent with early-time capillary theory, which predicts higher rates of uptake with increasing aperture width (Cheng et al., 2015; Shi et al., 2018). Under the overriding influence of capillarity, water experiences less sidewall friction and can move more easily within a wide fracture than a narrow one. This transient behavior is in sharp contrast to late-time capillary theory, which predicts a greater equilibrium height in narrow vs. wide fractures.

Mean values of the W_r for the different rock types ranged from 1.62 $m^2\ m^{-2}$ for CS to 1.88 $m^2\ m^{-2}$ for VBA (Table 1). The ANOVA indicated a significant effect of rock type on this property at $p < 0.05$. The granites generally had higher mean W_r values than the sedimentary rocks and yielded the lowest fracture sorptivity values, whereas the fracture surfaces of the sedimentary rocks were relatively smoother and yielded higher S_f values. As a result, fracture sorptivity was negatively correlated with W_r (Fig. 8). This relationship indicates that S_f tends to decrease as fracture surface roughness increases.

While our experiments were not performed under saturated flow conditions, similar principles probably apply with regard to the influence of roughness on fluid flow. Low-porosity rocks were used, which inhibit spontaneous imbibition into the matrix during early-time uptake. Thus, water movement was largely restricted to the fracture zone. Under saturated conditions, as the roughness of the fracture surface increases, so does the friction, thereby decreasing the rate of flow. Figure 8 suggests that this is also the case for spontaneous imbibition.

In the current study, other than being wrapped in Kapton tape, the rock cores were not subjected to any confining pressure. Because fracture sorptivity may be relevant to deep subsurface conditions, further research involving the incorporation of confining pressures into the spontaneous imbibition experiments might be beneficial. Also, during the fracturing process used in this study, it was qualitatively observed that certain rock types required higher or lower compressive loads to induce failure, indicating variation in tensile strengths. Quantifying the tensile stress at failure would allow increased rock type characterization and provide a potential parameter to explain variations in fracture aperture width between cores.

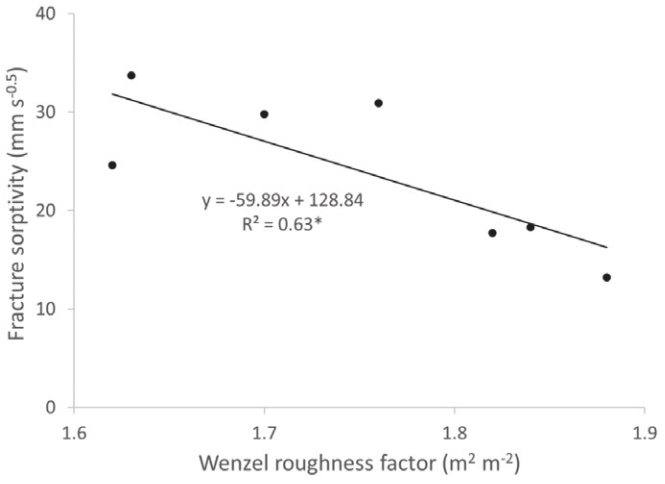

Fig. 8. Linear regression relationship between measured fracture sorptivity values and Wenzel surface roughness for all rock types.

A recent study by Vogler et al. (2017) suggested that, for smaller core sizes (less than ~2.5 cm in diameter), the Brazilian test tends to produce Mode I fractures dominated by intragranular cracks. Intragranular cracks can be expected to form jagged surfaces, thereby increasing roughness. A core diameter of 2.54 cm was used in the present study, and intragranular cracks were clearly visible on some of the granite fracture faces. The granites generally had the lowest sorptivity values, much lower than those predicted by Eq. [4]. We speculate that the sedimentary rocks, with smaller grain sizes, produced fractures following grain boundaries while the granites, with larger grain sizes, produced more jagged fracture surfaces due to the increased occurrence of intragranular cracks. This potential difference in how fractures propagate may explain some of the variations in the Wenzel roughness factor and fracture sorptivity values observed among the different rock types (see Table 1; Fig. 6).

Conclusions

This study provided measurements of spontaneous imbibition of water displacing air within individual fractures in a suite of low-porosity igneous and sedimentary rocks. Early-time uptake exhibited a square root of time dependency and was quantified in terms of fracture sorptivity, S_f. Estimates of S_f ranged from 10.1 to 40.5 mm $s^{-0.5}$, with a median value of 25.0 mm $s^{-0.5}$. There were statistically significant differences in mean fracture sorptivity between the rock types, with the igneous rocks generally having lower mean S_f values than the sedimentary rocks.

The rocks were characterized in terms of various physical properties, including bulk density, solid-phase density, porosity, contact angle, fracture aperture width, and fracture surface roughness. There were statistically significant differences in mean values among the rock types for all of the physical properties investigated. However, only the fracture aperture width and fracture surface roughness data were correlated with the S_f measurements. These correlations indicated that S_f increases with increasing fracture aperture width, as hypothesized based on early-time capillary theory, and that increasing fracture surface roughness decreases S_f, analogous to the well-known decrease in fracture permeability with increasing surface roughness under saturated flow conditions.

Acknowledgments

This research was sponsored by the Army Research Laboratory and was accomplished under Grant no. W911NF-16-1-0043. Portions of this research used resources at the High Flux Isotope Reactor, which is a USDOE Office of Science User Facility operated by Oak Ridge National Laboratory. E. Perfect acknowledges support from the Tom Cronin and Helen Sestak Faculty Achievement award. The solid-phase density, dry bulk density, and porosity data were collected by A.D. Vial.

References

Ai, H., X. Li, S. Shi, Y. Zhang, and T. Liu. 2017. Measurement of Wenzel roughness factor by laser scanning confocal microscopy. RSC Adv. 7:7052–7059. doi:10.1039/C6RA26897H

Alfarge, D., M. Wei, and B. Bai. 2017. IOR methods in unconventional reservoirs of North America: Comprehensive review. In: SPE Western Regional Meeting, Bakersfield, CA. 23–27 Apr. 2017. Soc. Pet. Eng., Richardson, TX. doi:10.2118/185640-MS

Bao, J.W., and L.C. Wang. 2017. Capillary imbibition of water in discrete planar cracks. Constr. Build. Mater. 146:381–392. doi:10.1016/j.conbuildmat.2017.04.129

Bizjak, K.F. 2010. Determining the surface roughness coefficient by 3D scanner. Geologija 53:147–152. doi:10.5474/geologija.2010.012

Brace, W.F., J.B. Walsh, and W.T. Frangos. 1968. Permeability of granite under high pressure. J. Geophys. Res. 73:2225–2236. doi:10.1029/JB073i006p02225

Brown, S.R. 1987. Fluid flow through rock joints: The effect of surface roughness. J. Geophys. Res. 92(B2):1337–1347. doi:10.1029/JB092iB02p01337

Cheng, C.L., E. Perfect, B. Donnelly, H.Z. Bilheux, A.S. Tremsin, L.D. McKay, et al. 2015. Rapid imbibition of water in fractures within unsaturated sedimentary rock. Adv. Water Resour. 77:82–89. doi:10.1016/j.advwatres.2015.01.010

Cui, C.J., M.W. Mozur, U.E. Verre, and F.N. Weltge. 2014. Unconventional and conventional hydrocarbon resource economics: A look at the fundamental differences and how countries can address the needs of unconventional resource exploitation. In: SPE Hydrocarbon Economics and Evaluation Symposium, Houston, TX. 19–20 May 2014. Soc. Pet. Eng., Richardson, TX. doi:10.2118/169873-MS

Culligan, P.J., V. Ivanov, and J.T. Germaine. 2005. Sorptivity and liquid infiltration into dry soil. Adv. Water Resour. 28:1010–1020. doi:10.1016/j.advwatres.2005.04.003

Dehghanpour, H., Q. Lan, Y. Saeed, H. Fei, and Z. Qi. 2013. Spontaneous imbibition of brine and oil in gas shales: Effect of water adsorption and resulting microfractures. Energy Fuels 27:3039–3049. doi:10.1021/ef4002814

DiStefano, V.H., M.C. Cheshire, J. McFarlane, L.M. Kolbus, R.E. Hale, E. Perfect, et al. 2017. Spontaneous imbibition of water and determination of effective contact angles in the Eagle Ford Shale Formation using neutron imaging. J. Earth Sci. 28:874–887.

Donnelly, B., E. Perfect, L.D. McKay, P.J. Lemiszki, V.H. DiStefano, L.M. Anovitz, et al. 2016. Capillary pressure– saturation relationships for gas shales measured using a water activity meter. J. Nat. Gas Sci. Eng. 33:1342–1352. doi:10.1016/j.jngse.2016.05.014

Gates, C.H., E. Perfect, B.S. Lokitz, J.W. Brabazon, L.D. McKay, and J.S. Tyner. 2018. Transient analysis of advancing contact angle measurements on polished rock surfaces. Adv. Water Resour. 119:142–149. doi:10.1016/j.advwatres.2018.03.017

Gaurina-Međimurec, N., and K.N. Mavar. 2017. Depleted hydrocarbon reservoirs and CO_2 injection wells: CO_2 leakage assessment. Rud.-Geol.-Naftni Zb. 32:15–26. doi:10.17794/rgn.2017.2.3

Gehne, S., and P.M. Benson. 2017. Permeability and permeability anisotropy in Crab Orchard sandstone: Experimental insights into spatio-temporal effects. Tectonophysics 712–713:589–599. doi:10.1016/j.tecto.2017.06.014

Ghanbari, E., and H. Dehghanpour. 2016. The fate of fracturing water: A field and simulation study. Fuel 163:282–294. doi:10.1016/j.fuel.2015.09.040

Hall, C. 1989. Water sorptivity of mortars and concretes: A review. Mag. Concr. Res. 41:51–61. doi:10.1680/macr.1989.41.147.51

Hall, S.A. 2013. Characterization of fluid flow in a shear band in porous rock using neutron radiography. Geophys. Res. Lett. 40:2613–2618. doi:10.1002/grl.50528

Huang, N., R.C. Liu, and Y.J. Jiang. 2017. Numerical study of the geometrical and hydraulic characteristics of 3D self-affine rough fractures during shear. J. Nat. Gas Sci. Eng. 45:127–142. doi:10.1016/j.jngse.2017.05.018

Huang, N., R.C. Liu, Y.Y. Jiang, B. Li, and L.Y. Yu. 2018. Effects of fracture surface roughness and shear displacement on geometrical and hydraulic properties of three-dimensional crossed rock fracture models. Adv. Water Resour. 113:30–41. doi:10.1016/j.advwatres.2018.01.005

Intergovernmental Panel on Climate Change. 2005. IPCC special report on carbon dioxide capture and storage. Cambridge Univ. Press, Cambridge, UK.

Kanematsu, M., I. Maruyama, T. Noguchi, H. Iikura, and N. Tsuchiya. 2009. Quantification of water penetration into concrete through cracks by neutron radiography. Nucl. Instrum. Methods Phys. Res. A 605:154–158. doi:10.1016/j.nima.2009.01.206

Karpyn, Z.T., P.M. Halleck, and A.S. Grader. 2009. An experimental study of spontaneous imbibition in fractured sandstone with contrasting sedimentary layers. J. Pet. Sci. Eng. 67:48–56. doi:10.1016/j.petrol.2009.02.014

Keller, A. 1998. High resolution, non-destructive measurement and characterization of fracture apertures. Int. J. Rock Mech. Min. Sci. 35:1037–1050. doi:10.1016/S0148-9062(98)00164-8

Kim, J.-S., S.-K. Kwon, M. Sanchez, and G.-C. Cho. 2011. Geological storage of high level nuclear waste. KSCE J. Civ. Eng. 15:721–737. doi:10.1007/s12205-011-0012-8

Konzuk, J.S., and B.H. Kueper. 2004. Evaluation of cubic law based models describing single-phase flow through a rough-walled fracture. Water Resour. Res. 40:W02402. doi:10.1029/2003WR002356

Koyama, T., B. Li, Y. Jiang, and L. Jing. 2008. Numerical simulations for the effects of normal loading on particle transport in rock fractures during shear. Int. J. Rock Mech. Min. Sci. 45:1403–1419. doi:10.1016/j.ijrmms.2008.01.018

Li, D.Y., and L.N.Y. Wong. 2013. The Brazilian disc test for rock mechanics applications: Review and new insights. Rock Mech. Rock Eng. 46:269–287. doi:10.1007/s00603-012-0257-7

Li, Q., H. Xing, J. Liu, and X. Liu. 2015. A review on hydraulic fracturing of unconventional reservoir. Petroleum 1:8–15. doi:10.1016/j.petlm.2015.03.008

Lockington, D.A., C. Leech, J.-Y. Parlange, and P.F. Dux. 2002. The sorptivity test and predicting resistance to water absorption in concrete. In: R.K. Dhir et al., editors, Innovations and developments in concrete materials and construction. ICE Publ., London. p. 315–324.

Mokhtari, M., and A.N. Tutuncu. 2015. Characterization of anisotropy in the permeability of organic-rich shales. J. Pet. Sci. Eng. 133:496–506. doi:10.1016/j.petrol.2015.05.024

Morrow, N.R., and G. Mason. 2001. Recovery of oil by spontaneous imbibition. Curr. Opin. Colloid Interface Sci. 6:321–337. doi:10.1016/S1359-0294(01)00100-5

Navarre-Sitchler, A., S.L. Brantley, and G. Rother. 2015. How porosity increases during incipient weathering of crystalline silicate rocks. Rev. Mineral. Geochem. 80:331–354. doi:10.2138/rmg.2015.80.10

Onda, T., S. Shibuichi, N. Satoh, and K. Tsujii. 1996. Super-water-repellent fractal surfaces. Langmuir 12:2125–2127. doi:10.1021/la950418o

Osiptsov, A.A. 2017. Fluid mechanics of hydraulic fracturing: A review. J. Pet. Sci. Eng. 156:513–535. doi:10.1016/j.petrol.2017.05.019

Perfect, E., C.L. Cheng, M. Kang, H.Z. Bilheux, J.M. Lamanna, M.J. Gragg, and D.M. Wright. 2014. Neutron imaging of hydrogen-rich fluids in geomaterials and engineered porous media: A review. Earth Sci. Rev. 129:120–135. doi:10.1016/j.earscirev.2013.11.012

Philip, J.R. 1957. The theory of infiltration: 4. Sorptivity and algebraic infiltration equations. Soil Sci. 84:257–264. doi:10.1097/00010694-195709000-00010

R Core Team. 2016. R: A language and environment for statistical computing. R Found. Stat. Comput., Vienna. https://www.R-project.org/

Ramón-Torregrosa, P.J., M.A. Rodríguez-Valverde, A. Amirfazli, and M.A. Cabrerizo-Vílchez. 2008. Factors affecting the measurement of roughness factor of surfaces and its implications for wetting studies. Colloids Surf. A 323:83–93. doi:10.1016/j.colsurfa.2007.10.032

Rangel-German, E.R., and A.R. Kovscek. 2002. Experimental and analytical study of multidimensional imbibition in fractured porous media. J. Pet. Sci. Eng. 36:45–60. doi:10.1016/S0920-4105(02)00250-4

Rossi, A.M., and R.C. Graham. 2010. Weathering and porosity formation in subsoil granitic clasts, Bishop Creek moraines, California. Soil Sci. Soc. Am. J. 74:172–185. doi:10.2136/sssaj2009.0146

Şahmaran, M., and V.C. Li. 2009. Influence of microcracking on water absorption and sorptivity of ECC. Mater. Struct. 42:593–603. doi:10.1617/s11527-008-9406-6

Schmid, K.S., S. Geiger, and K.S. Sorbie. 2011. Semianalytical solutions for cocurrent and countercurrent imbibition and dispersion of solutes in immiscible two-phase flow. Water Resour. Res. 47:W02550. doi:10.1029/2010WR009686

Schmid, K.S., and S. Geiger. 2012. Universal scaling of spontaneous imbibition for water-wet systems. Water Resour. Res. 48:W03507. doi:10.1029/2011WR011566

Schneider, C.A., W.S. Rasband, and K.W. Eliceiri. 2012. NIH Image to ImageJ: 25 years of image analysis. Nat. Methods 9:671–675. doi:10.1038/nmeth.2089

Schwiebert, M.K., and W.H. Leong. 1996. Underfill flow as viscous flow between parallel plates driven by capillary action. IEEE Trans. Compon., Packag., Manuf. Technol., Part C 19:133–137. doi:10.1109/3476.507149

Shi, Y., M.R. Yassin, and H. Dehghanpour. 2018. A modified model for spontaneous imbibition of wetting phase into fractal porous media. Colloids Surf. A 543:64–75. doi:10.1016/j.colsurfa.2017.12.052

Suzuki, A., S. Fomin, V. Chugunov, and T. Hashida. 2018. Mathematical modeling of non-Fickian diffusional mass exchange of radioactive contaminants in geological disposal formations. Water 10(2):123. doi:10.3390/w10020123

Taha, M.M.R., A.S. El-Dieb, and N.G. Shrive. 2001. Sorptivity: A reliable measurement for surface absorption of masonry brick units. Mater. Struct. 34:438–445. doi:10.1007/BF02482291

Vengosh, A., R.B. Jackson, N. Warner, T.H. Darrah, and A. Kondash. 2014. A critical review of the risks to water resources from unconventional shale gas development and hydraulic fracturing in the United States. Environ. Sci. Technol. 48:8334–8348. doi:10.1021/es405118y

Vogler, D., S.D.C. Walsh, P. Bayer, and F. Amann. 2017. Comparison of surface properties in natural and artificially generated fractures in a crystalline rock. Rock Mech. Rock Eng. 50:2891–2909. doi:10.1007/s00603-017-1281-4 [erratum: 51:359. doi:10.1007/s00603-017-1361-5]

Wanless, H.R. 1946. Pennsylvanian geology of a part of the southern Appalachian coal field. Geol. Soc. Am. Mem. 13. doi:10.1130/MEM13-p1

Wenzel, R.N. 1936. Resistance of solid surfaces to wetting by water. Ind. Eng. Chem. 28:988–994. doi:10.1021/ie50320a024

Ye, Z., and A. Ghassemi. 2018. Experimental study on injection-induced fracture propagation and coalescence for EGS stimulation. In: Proceedings: 43rd Workshop on Geothermal Reservoir Engineering, Stanford, CA. Tech. Rep. SGP-TR-213. Stanford Univ., Stanford, CA.